

Recovering 21cm global signal from 21cm power spectrum with artificial neural network

Hayato Shimabukuro

Yunnan University, SWIFAR, No.2 North Green Lake Road, Kunming, Yunnan Province, 650500, China
Graduate School of Science, Division of Particle and Astrophysical Science,

*Nagoya University, Chikusa-Ku, Nagoya, 464-8602, Japan**

(Dated: December 31, 2024)

In this paper, we propose a novel method to recover the 21cm global signal from the 21cm power spectrum using artificial neural networks (ANNs). The 21cm global signal is crucial for understanding cosmic evolution from the Dark Ages through the Epoch of Reionization (EoR). While interferometers like LOFAR, MWA, HERA, and SKA focus on detecting the 21cm power spectrum, single-dish experiments such as EDGES target the global signal. Our method utilizes ANNs to establish a connection between these two observables, providing a means to cross-validate independent 21cm line observations. This capability is significant as it allows different observational approaches to verify each other's results, ensuring greater reliability in 21cm cosmology. We demonstrate that our ANN-based approach can accurately recover the 21cm global signal across a wide redshift range ($z = 7.5\text{--}35$) from simulated data, even when realistic thermal noise levels, such as those expected from SKA-1, are considered. This cross-validation process strengthens the robustness of 21cm signal analysis, offering a more comprehensive understanding of the early universe.

I. INTRODUCTION

Following the cosmic “dark ages,” during which no luminous objects existed, the universe witnessed the formation of the first stars and galaxies in a period known as the “cosmic dawn” [e.g. 1]. The X-ray and ultraviolet (UV) photons emitted by these early luminous objects heated and ionized the neutral hydrogen atoms in the intergalactic medium (IGM) [e.g. 2], leading to the epoch of reionization (EoR), which persisted until the IGM was fully ionized.

The redshifted 21cm line signal from neutral hydrogen is a promising probe for studying the history of the universe from the Dark Ages through the EoR. This signal arises from the hyperfine transition of neutral hydrogen atoms and can provide direct tomographic images of the spatial distribution of HI gas in the IGM [e.g. 2, 3, 4, 5]. Creating three-dimensional maps of this distribution requires high sensitivity and spatial resolution. As an alternative, current radio interferometer arrays, such as LOFAR (Low Frequency Array) [e.g. 6], the Murchison Widefield Array (MWA) [e.g. 7], and the Hydrogen Epoch of Reionization Array (HERA) [e.g. 8], aim to statistically detect the 21cm line signal by measuring its power spectrum. These arrays have already set upper limits on the 21cm line power spectrum [e.g., see Fig. 19 of 9], and future experiments, such as the Square Kilometre Array (SKA) [10, 11], promise to achieve even higher sensitivity.

Single-dish radio telescopes, such as the Experiment to Detect the Global Epoch of Reionization Signature (EDGES) [12], the Large-aperture Experiment to Detect the Dark Ages (LEDA) [13], the Probing Radio Intensity

at High-Z from Marion (PRIZM)[14], and the Shaped Antenna measurement of the background RAdio Spectrum (SARAS)[15, 16], focus on measuring the global 21cm signal, which is the sky-averaged 21cm line signal.

Different from ground-based telescopes, which are affected by Earth's radio frequency interference and atmospheric absorption, lunar-based or lunar-orbiting telescopes offer significant advantages for detecting the faint 21cm global signal. The farside of the Moon provides a radio-quiet environment, free from Earth's radio frequency interference, making it an ideal location for such sensitive observations. Additionally, the lack of an atmosphere eliminates signal absorption and scattering, allowing for more precise measurements. Currently, several projects for lunar-based or lunar-orbiting telescopes have been proposed, including FarView[17], LuSEE-night[18], PRATUSH[19], Discovering the Sky at the Longest Wavelength (DSL)[20] and Large-scale Array for Radio Astronomy on the Farside(LARAF)[21].

Unlike the power spectrum, this global signal is a spatially invariant measurement. The EDGES team has reported a detection of a 21cm absorption trough at cosmic dawn ($z \sim 17$) [12]. However, the depth of this absorption trough is challenging to reconcile with standard cosmological and astrophysical models, prompting suggestions of non-standard scenarios, such as interactions with dark matter or an excess radio background [e.g. 22, 23]. The SARAS3 experiment independently contested the EDGES results, ruling them out with a 95.3%

Traditionally, the global 21cm signal has been measured using single-dish radio telescopes rather than radio interferometers. Single-dish experiments are well-suited for this purpose because they can capture the sky-averaged signal over a broad field of view, providing a direct measurement of the global 21cm signal. In contrast, radio interferometers, which consist of multiple antennas working together, measure the differences in the signals

*Electronic address: shimabukuro@ynu.edu.cn

received by pairs of antennas. This configuration makes interferometers highly sensitive to spatial variations in the signal but not to the spatially invariant global signal.

The global 21cm signal is a sky-averaged measure, representing the mean temperature of the neutral hydrogen across the entire sky at a given redshift. To directly measure this signal using an interferometer, one would need to achieve a baseline length of zero ($u = v = 0$ in the uv-plane), which is equivalent to having the antennas at the same location. This is practically impossible because interferometers are designed to have antennas spread out over distances to achieve high spatial resolution.

Instead, interferometers excel at mapping the 3D structure of the 21cm signal, capturing fluctuations in the hydrogen distribution with high sensitivity and spatial resolution. These fluctuations are encoded in the 21cm power spectrum, which describes the intensity of variations at different scales[e.g. 24]. Several methods have been proposed to measure the global signal with interferometers indirectly. These methods often involve sophisticated techniques to extract the global signal from interferometric data. Still, they face challenges due to the inherent differences in what interferometers and single-dish experiments measure[25, 26, 27, 28]. In summary, while single-dish experiments provide a more straightforward approach to measuring the global 21cm signal, radio interferometers offer complementary capabilities through their ability to map spatial fluctuations in hydrogen distribution. Combining insights from both types of observations can enhance our understanding of the 21cm signal and its implications for the early universe.

The 21cm power spectrum and the global signal are independent observables, each providing unique insights into the universe's evolution during the cosmic dawn and the Epoch of Reionization (EoR). The 21cm power spectrum captures the spatial fluctuations in the brightness temperature of neutral hydrogen, offering a detailed map of the structure of the IGM at different scales. In contrast, the global signal represents the sky-averaged brightness temperature, providing a broad overview of the thermal and ionization history of the IGM. The synergy between these two observables is crucial for cross-validation and a comprehensive understanding of 21cm measurements.

Recent studies, such as those by Cohen et al. [29] and Fialkov et al. [30], have highlighted the potential synergy between these two observables. Cohen et al. [29] explored a wide range of astrophysical parameters that affect the 21cm power spectrum, demonstrating that features in the power spectrum can infer global signal characteristics and significant cosmic events. The slope of the power spectrum, which exhibits a more universal redshift evolution, can trace high-redshift astrophysics more easily and provide consistency checks against the global signal. Fialkov et al. [30] proposed a technique that constructs the global signal from the ratio of 21cm fluctuations to the fluctuations in the number of galaxies, which trace the underlying matter density at the same locations. This

multi-tracer approach allows us to cross-correlate different datasets, thereby reducing the impact of noise and systematics that might affect a single type of measurement. By tracing both the 21cm fluctuations and the corresponding matter density fluctuations, the method can provide a more accurate reconstruction of the global signal.

Recently, machine learning techniques, particularly artificial neural networks (ANNs), have been applied to study the 21cm signal from the Dark Ages to cosmic reionization. ANNs have been used for parameter estimation [e.g. 31, 32, 33], emulator construction [e.g. 34, 35, 36, 37], generating 21cm line maps from galaxy distributions[38], and separating EoR signals from foreground noise[39]. Additionally, ANNs have the potential to recover ionized bubble size distributions from the 21cm power spectrum[40]. In conjunction with these machine learning techniques, simulation-based inference (SBI) has emerged as a powerful approach for studying the 21cm signal. SBI leverages simulations to model complex processes underlying the 21cm signal, enabling accurate inference of astrophysical parameters[e.g. 41, 42]. For example, Zhao et al. [41] used density-estimation likelihood-free inference (DELFI) with 3D convolutional neural networks (3D CNNs) to infer reionization parameters with posterior from 21cm images.

In this paper, we propose a novel method to recover the 21cm global signal from the 21cm power spectrum using an artificial neural network (ANN). Our approach trains the ANN to map the relationship between the power spectrum and the global signal. This method is robust against observational noise and can validate results from single-dish experiments like EDGES by providing independent measurements. This cross-validation enhances the reliability of 21cm cosmology studies and deepens our understanding of the early universe.

II. COSMOLOGICAL 21CM SIGNAL

The fundamental observable for the 21cm signal is the brightness temperature, which can be expressed as:[e.g. 10]

$$\begin{aligned} \delta T_b(\nu) &= \frac{T_S - T_\gamma}{1 + z} (1 - e^{-\tau_{\nu_0}}) \\ &\sim 27 x_H (1 + \delta_m) \left(\frac{H}{dv_r/dr + H} \right) \left(1 - \frac{T_\gamma}{T_S} \right) \\ &\times \left(\frac{1 + z}{10} \frac{0.15}{\Omega_m h^2} \right)^{1/2} \left(\frac{\Omega_b h^2}{0.023} \right) \left(\frac{\Omega_b h}{0.031} \right) [\text{mK}]. \end{aligned} \quad (1)$$

where T_S and T_γ represent the spin temperature of the IGM and CMB temperature, respectively. The optical depth in 21cm rest frame at frequency $\nu_0 = 1.4\text{GHz}$ is denoted by τ_{ν_0} . The neutral fraction of hydrogen atom is given by x_H and $\delta_m(\mathbf{x}, z) \equiv \rho/\bar{\rho} - 1$ represents matter

density fluctuations. The velocity gradient of the IGM along the line of sight is represented by dv_r/dr , and H is the Hubble parameter. All parameters are evaluated at redshift $z = \nu_0/\nu - 1$. Other parameters include cosmological parameters.

For practical purposes, it's often more convenient to analyze 21cm fluctuations in Fourier space. The 21cm fluctuations are typically evaluated using the 21cm line power spectrum, defined as: [e.g. 2]

$$\langle \delta T_b(\mathbf{k}) \delta T_b(\mathbf{k}') \rangle = (2\pi)^3 \delta(\mathbf{k} + \mathbf{k}') P_{21}(\mathbf{k}). \quad (2)$$

where the dimensionless 21cm line power spectrum is expressed as $k^3 P_{21}(k)/2\pi^2$. In the study, we employ a semi-numerical simulation approach, similar to that used in Cohen et al. [29, 43] to calculate the 21cm line power spectrum. For more detailed modeling please refer to these foundation studies.

III. ARTIFICIAL NEURAL NETWORKS

In this section, we introduce artificial neural networks (ANNs), a class of machine learning methods inspired by the neural networks in the human brain. ANNs are primarily designed to construct approximate functions that map input data to output data, which requires training using *training data*." A simple ANN architecture consists of three layers: the input layer, the hidden layer, and the output layer, each containing a number of neurons. In more complex cases, the number of hidden layers and neurons in each layer can be varied.

In our study, we use a dataset where the input is the 21cm power spectrum (PS) and the output is the global signal. Specifically, we use the 21cm PS as a function of redshift at a fixed wavenumber k . The redshift range for both the 21cm line power spectrum and the global signal is $z = 7.5 - 35$, divided into 95 bins. Accordingly, we assign 95 neurons to both the input and output layers, corresponding to these redshift bins. The 21cm PS is considered at fixed wavenumber $k = 0.1, 0.5, \text{ and } 1.0 \text{ Mpc}^{-1}$, meaning there are equal numbers of 21cm power spectra and global signals. We use 5 hidden layers, each with 95 neurons.

The architecture of our ANN is briefly described as follows. The input data x_j is fed to the j -th neuron in the input layer. Each input neuron is connected to the i -th neuron in the hidden layer with a weight $w_{ij}^{(1)}$ associated with each connection. The i -th neuron in the hidden layer, s_i , is expressed as a linear combination of all input neurons with their respective weights $w_{ij}^{(1)}$:

$$s_i = \sum_{j=1}^n w_{ij}^{(1)} x_j, \quad (3)$$

where n is the number of input data points. In the hidden layer, the i -th neuron is activated by an activation

function ϕ , producing the output $t_i = \phi(s_i)$. We use the ReLU function as the activation function, defined as follows:

$$\phi(x) = \max(0, x) = \begin{cases} x & (x \geq 0) \\ 0 & (x < 0) \end{cases} \quad (4)$$

In the output layer, the output vector is obtained by computing linear combinations of the activated neurons in the hidden layer with weights $w_{ij}^{(L)}$ (where L denotes the total number of layers):

$$y_i = \sum_{j=1}^k w_{ij}^{(L)} t_j, \quad (5)$$

where k is the number of neurons in the hidden layer. Note that the output values are not activated. The goal of training the ANN is to find a set of weights that ensures the output vectors produced by the ANN for a set of input vectors are close to the desired output vectors. Once the weights are adjusted to minimize the difference using a training sample, the ANN can predict output vectors for new input vectors outside the training sample, such as new observational data. To quantify the accuracy of the ANN's output relative to the desired output for the training data, we define the total cost function as:

$$E = \sum_{n=1}^{N_{\text{train}}} E_n = \sum_{n=1}^{N_{\text{train}}} \left[\frac{1}{2} \sum_{i=1}^m (y_{i,n} - d_{i,n})^2 \right], \quad (6)$$

where N_{train} is the number of training datasets, and m is the number of neurons in the output layer. y and d represent the outputs of the ANN and the desired training output data, respectively. Our objective is to minimize the cost function by finding the optimal set of weights. This is achieved by computing the partial derivatives of E concerning the individual weights $w_{ij}^{(l)}$ and finding the local minimum of E using gradient descent. We employ the "backpropagation algorithm" to compute the trained weights [44]. For readers in the details of the backpropagation algorithm, please refer to [31].

IV. RESULTS

In this section, we present the global signal recovered from the 21cm line power spectrum as a function of redshift using the ANN. We performed the backpropagation algorithm with 20,000 iterations for 400 training datasets and then applied the trained network to 100 test datasets. Before discussing the main results, we evaluate whether the training of the ANN architecture is adequate. To do this, we calculated the mean square error (MSE) of the training dataset, defined as

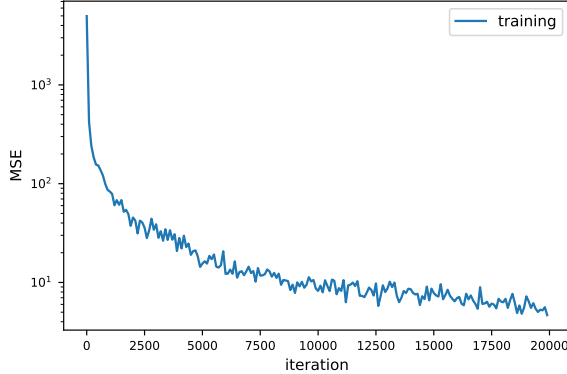


FIG. 1: The mean square error (MSE) between obtained and target values in the training dataset. The MSE converges after 20'000 iterations.

$$\text{MSE} = \frac{1}{N_{\text{train}}} \sum_{i=1}^{N_{\text{train}}} E_n \quad (7)$$

In Fig. 1, we show the MSE as a function of the number of iterations. We show the MSE as a function of the number of iterations. We found that the MSE converged after 20,000 iterations. Therefore, we used 20,000 iterations for the backpropagation in subsequent calculations.

A. Recovered 21cm global signal

We recover 21cm global signal at $z = 7.5 - 35$ redshift from the 21cm PS as a function of redshift. We use the 21cm PS at a fixed wavenumber $k = 0.1\text{Mpc}^{-1}$. In Fig.2, We compare the true global signal with the one recovered using the ANN from the 21cm power spectrum over this redshift range. As seen in Fig.2, the ANN successfully reconstructs the global signal from cosmic dawn to EoR.

Previous studies, such as [30], have demonstrated that multi-tracer methods can extract the global signal using both 21cm and matter density fluctuations. However, our method, which is based on an ANN, requires only the 21cm fluctuations. The ANN efficiently learns a non-linear mapping between the 21cm power spectrum and the global signal, effectively functioning as a non-linear regression tool that eliminates the need for additional tracers. By training on simulated datasets, the ANN approximates the complex relationship between the 21cm PS input and the global signal, allowing for accurate recovery.

To assess the ANN's performance across all test data, we compare the recovered and true global signals at the trough of the 21cm global signal for all test cases. In Fig.3, we examine the depth of the trough in the recovered global signal across all test datasets, with the $Y = X$

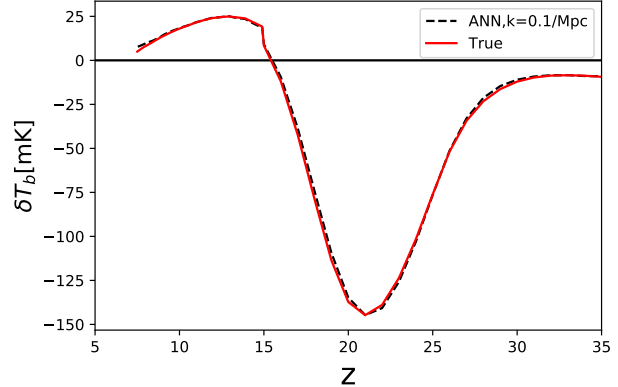


FIG. 2: True 21cm global signal(*red solid*) and recovered 21cm global signal from 21cm line power spectrum from EoR to cosmic dawn($z=7.5-35$)(*black dashed*).

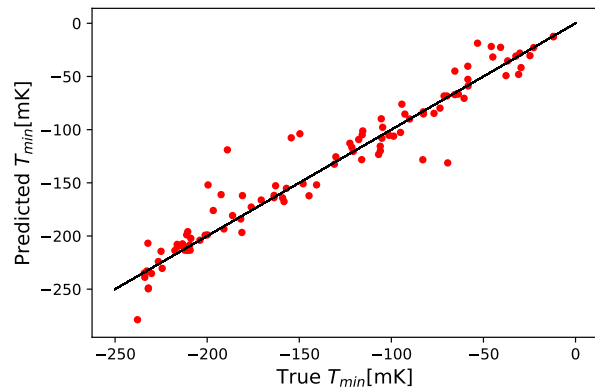


FIG. 3: Comparison of depth of trough between obtained and true global signal values for all test datasets. The solid black line ($Y=X$) represents perfect prediction.

line representing perfect recovery. As shown in the figure, the ANN successfully recovers the depth of the global signal at the trough from the 21cm power spectrum, closely matching the true values. This demonstrates that the model generalizes well across test datasets.

To quantitatively assess the accuracy of the recovered global 21cm signal across all test datasets, we introduce the correlation coefficient (CC), defined as:

$$\text{CC} = \frac{\sum_{i=1}^{N_z} (y_{\text{true},i} - \bar{y}_{\text{true}})(y_{\text{ANN},i} - \bar{y}_{\text{ANN}})}{\sqrt{\sum_{i=1}^{N_z} (y_{\text{true},i} - \bar{y}_{\text{true}})^2} \sqrt{\sum_{i=1}^{N_z} (y_{\text{ANN},i} - \bar{y}_{\text{ANN}})^2}} \quad (8)$$

where $y_{\text{true},i}$ and $y_{\text{ANN},i}$ represent the true and recovered values of the global signal at redshift z_i , respectively, and N_z is the number of redshift bins. The overbars denote mean values averaged over all redshifts. The CC measures the linear correlation between the true and recovered signals for each test dataset; a CC close to 1 indi-

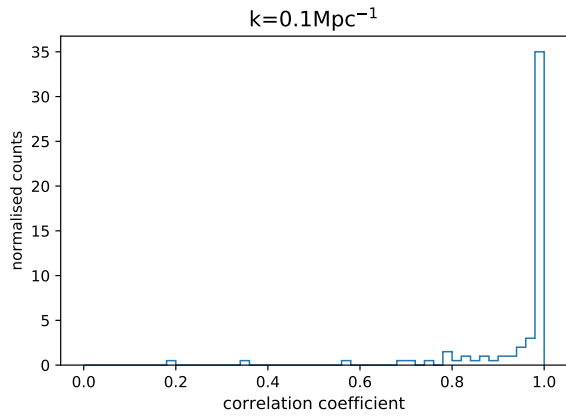


FIG. 4: Distribution of the correlation coefficient (CC) for all test datasets where the global signal is recovered from the 21cm PS at $k = 0.1\text{Mpc}^{-1}$. The mean value is 0.95, and the variance is 0.05.

cates a strong positive correlation, while a CC close to -1 indicates a strong negative correlation. A higher absolute value of CC signifies a stronger correlation between the datasets.

We first compute the CC for the case where the 21cm global signal is recovered from the 21cm power spectrum (PS) at $k = 0.1\text{Mpc}^{-1}$. As shown in Fig.4, most of the CC values are distributed between 0.8 and 1.0, with a mean of 0.95 and a variance of 0.05. This quantitatively demonstrates that our artificial neural network (ANN) can successfully recover the 21cm global signal from the 21cm PS at $k = 0.1\text{Mpc}^{-1}$ for most of the models we consider. However, for some models, the CC values are less than 0.6, indicating that the recovery does not perform as well for these cases compared to others. This can be attributed to the following reasons. In certain models, the 21cm power spectrum at specific scales (i.e. $k = 0.1\text{Mpc}^{-1}$) does not contain enough information to accurately recover the global signal. This is particularly evident when the power spectrum exhibits anomalies, such as missing the typical three peaks or showing significant shifts in peak positions. Such irregularities hinder the ANN’s ability to effectively learn the relationship between the power spectrum and the global signal.

Next, we investigate how the scale of the 21cm line power spectrum used for the ANN affects recovering the 21cm global signal. In Fig.5, we present the recovered global signal and the corresponding 21cm PS as functions of redshift for fixed wavenumbers $k = 0.1, 0.5,$ and 1.0Mpc^{-1} . The top panel illustrates that the recovery of the global signal deteriorates when using the 21cm PS at $k = 1.0\text{Mpc}^{-1}$. The bottom panel shows that while the 21cm PS at $k = 0.1$ and 0.5Mpc^{-1} exhibit three peaks as functions of redshift, the PS at $k = 1.0\text{Mpc}^{-1}$ displays only two peaks. Additionally, the redshift of the middle peak ($z \sim 17$) differs between the $k = 1.0\text{Mpc}^{-1}$ case and the lower k cases.

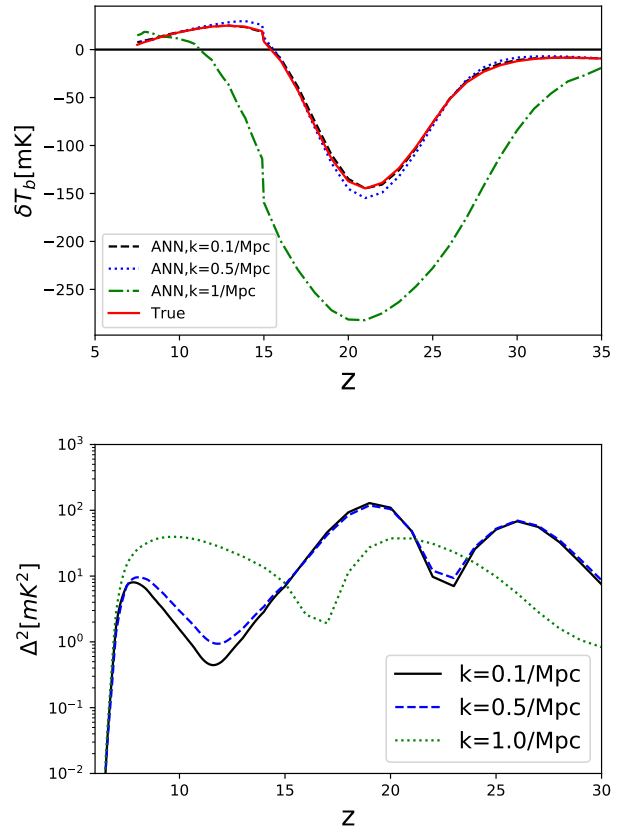


FIG. 5: (Top) The global 21cm signal recovered using the 21cm PS at fixed wavenumbers $k = 0.1, 0.5,$ and 1.0Mpc^{-1} . (Bottom) The corresponding 21cm PS as functions of redshift at the same fixed wavenumbers. Note that the recovery deteriorates at $k = 1.0\text{Mpc}^{-1}$, where the PS exhibits only two peaks instead of three.

These differences suggest that the reduced accuracy in recovering the global signal from the 21cm PS at $k = 1.0\text{Mpc}^{-1}$ is due to the loss of critical information about the global signal at smaller scales. Since the global signal represents the sky-averaged 21cm emission, it inherently contains large-scale information, and small-scale fluctuations average out in the process. Therefore, using the 21cm PS at smaller scales (higher k) may not capture the necessary information to accurately recover the global signal.

To further evaluate the impact of the PS scale on the recovery accuracy, we compute the CC for the cases using the 21cm PS at $k = 0.1, 0.5,$ and 1.0Mpc^{-1} , as shown in Fig. 6. For $k = 0.1$ and 0.5Mpc^{-1} , the majority of CC values are greater than 0.75, indicating a strong correlation between the true and recovered global signals. In contrast, for $k = 1.0\text{Mpc}^{-1}$, the CC values are widely distributed between 0 and 1, with a mean of 0.18 and a variance of 0.27. This result reinforces the notion that the recovery of the global signal is less effective when relying solely on smaller scales of the 21cm PS.

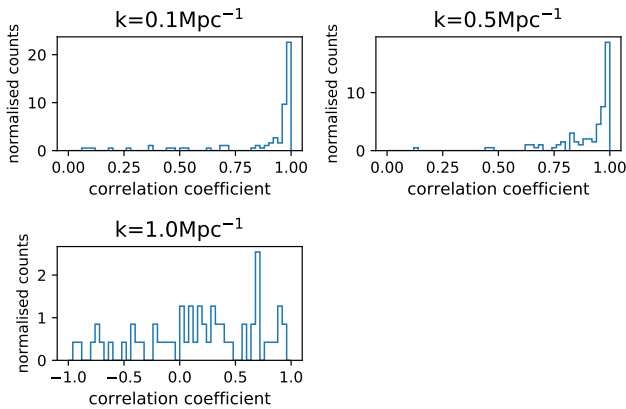


FIG. 6: Distribution of the correlation coefficient (CC) for all test datasets where the global signal is recovered from the 21cm PS at different fixed wavenumbers $k = 0.1, 0.5,$ and 1.0Mpc^{-1} . The mean CC values are 0.95, 0.88, and 0.18, respectively, with variances of 0.05, 0.18, and 0.27. The recovery accuracy decreases significantly at $k = 1.0 \text{Mpc}^{-1}$.

Returning to Fig.4, we note that some CC values are less than 0.6 even when using the 21cm PS at $k = 0.1 \text{Mpc}^{-1}$. In these particular models, the 21cm PS as a function of redshift at $k = 0.1 \text{Mpc}^{-1}$ exhibits only two peaks instead of the typical three. This reduction in the number of peaks suggests a loss of information content in the PS, which hinders the ANN’s ability to recover the global signal accurately. Therefore, the insufficient extraction of information from the PS in these models leads to a lower CC and poorer recovery performance.

Our analysis indicates that the accuracy of recovering the global 21cm signal using an ANN depends significantly on the scales of the 21cm PS employed. Larger scales (lower k) contain more relevant information about the global signal, as they are less affected by small-scale fluctuations that average out in the sky-averaged signal. Consequently, using the 21cm PS at smaller scales alone is insufficient for accurate recovery, and incorporating larger scales improves the performance of the ANN in reconstructing the global signal across various EoR models.

B. The recovery from the 21cm PS with thermal noise

So far, we have assumed that the input 21cm line power spectrum is the pure signal derived from simulations. However, in practical observations, measurements of the 21cm line power spectrum are contaminated by random noise. For large radio interferometer arrays like the Square Kilometre Array (SKA), thermal noise dominates the noise budget, although cosmic variance also contributes significantly at large scales. In this subsection, we incorporate both thermal noise and cosmic vari-

ance into our analysis to investigate their effects on the reconstruction of the global signal.

The thermal noise power spectrum for a single mode \mathbf{k} is given by [45, 46, 47]:

$$P_{\text{th,1mode}}(k, \mu) = d_A^2 y \frac{\Omega}{t} \frac{T_{\text{sys}}^2}{\bar{n}(Lk_{\perp})A_e}, \quad (9)$$

where $d_A(z)$ is the comoving angular diameter distance at redshift z , and $y(z) \equiv \lambda_{21}(1+z)^2/H(z)$, with $\lambda_{21} = \lambda(z)/(1+z) = 0.21 \text{m}$ and $H(z)$ being the Hubble parameter at z . The solid angle of the field of view is $\Omega = \lambda^2/A_e$, where λ is the observing wavelength and A_e is the effective area per station. The total integration time is t , and T_{sys} is the system temperature of the antenna, which is the sum of the receiver temperature (approximately 100K) and the sky temperature $T_{\text{sky}} = 60(\nu/300, \text{MHz})^{-2.55} \text{K}$. The term $\bar{n}(Lk_{\perp})A_e$ represents the number of redundant baselines with L corresponding to k_{\perp} within a baseline area equal to A_e .

The thermal noise for the mode \mathbf{k} depends on its projection onto the sky plane, $k_{\perp} = k\sqrt{1-\mu^2}$, where $\mu = \cos\theta$, and θ is the angle between the mode \mathbf{k} and the line of sight (LOS).

The thermal noise for the spherically averaged power spectrum over a k -shell is given by [48]:

$$P_{\text{thermal}}(k) = \left[\sum_{\mu} \frac{N_c(k, \mu)}{P_{\text{th,1mode}}^2(k, \mu)} \right]^{-1/2}, \quad (10)$$

where $N_c(k, \mu)$ is the number of modes in the ring with μ on the spherical k -shell with logarithmic step size $\delta k/k = \epsilon$. Specifically, $N_c(k, \mu) = \epsilon k^3 \Delta\mu \times \text{vol}/(4\pi^2)$, and vol is the survey volume of the sky. The summation accounts for the noise reduction achieved by combining independent modes. It runs over the upper half-shell with positive μ , since the brightness temperature field is real-valued, and only half of the Fourier modes are independent.

The cosmic variance for the 21cm line power spectrum is estimated by

$$P_{\text{cv}}(k) = \frac{1}{\sqrt{N_{\text{modes}}}} P_{21}(k), \quad (11)$$

where $N_{\text{modes}} = \epsilon k^3 \times \text{vol}/(4\pi^2)$ is the number of modes in the upper half of the k -shell.

In this study, we consider an experiment similar to the low-frequency array of SKA Phase 1 (SKA-1). Specifically, we assume a configuration where 224 stations are compactly arranged within a core diameter of 1000 meters, and the minimum baseline between stations is 60 meters. We adopt the following parameters: the field of view of a single primary beam is $\text{FWHM} \sim 3.5^\circ$ at $z \sim 8$, the effective area per station is $A_e \approx 421 \text{m}^2$ at $z \sim 8$, the total integration time is 1000 hours, the bandwidth of a redshift bin is 10MHz, and the logarithmic step size of a k -bin is $\epsilon = \delta k/k = 0.1$.

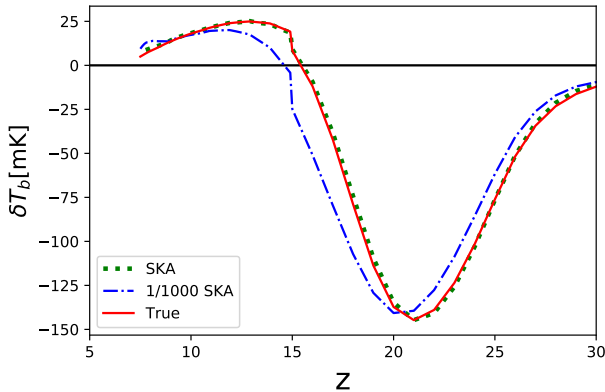


FIG. 7: Recovered global signal from noisy 21cm line power spectrum. The target global signal (*red solid line*), recovered signal assuming SKA-1 thermal noise (*green dotted line*), and recovered signal assuming thermal noise 1000 times larger than SKA-1 (*blue dot-dashed line*).

Our noise computation results are consistent with previous studies [e.g., 11]. For SKA-1, the cosmic variance is negligible, and the thermal noise is small compared to the signal for $k \leq 1\text{Mpc}^{-1}$. Consequently, the 21cm signal dominates over the noise except at small scales. This favorable signal-to-noise ratio allows for the effective reconstruction of the global signal even in the presence of noise.

We model the measured 21cm line power spectrum as

$$P(k) = P_{21}(k) + N(k), \quad (12)$$

where $P_{21}(k)$ is the true 21cm line power spectrum signal, and $N(k)$ is a random draw from a Gaussian distribution with zero mean and variance equal to the total noise power spectrum $P_N^2(k) = P_{\text{thermal}}^2(k) + P_{\text{cv}}^2(k)$.

In Fig.7, We present the global signal recovered from a noisy 21cm line power spectrum assuming SKA-1 experiment specifications. For comparison, we also show the recovered global signal from a 21cm PS with a thermal noise power spectrum that is 1000 times larger than that of SKA-1, which is roughly comparable to the noise levels of MWA or LOFAR [49]. Remarkably, we observe that the 21cm global signal can be adequately recovered from the 21cm PS even when the thermal noise is 1000 times higher than that of SKA-1. This indicates the robustness of our ANN-based recovery method against thermal noise. This result highlights the ANN’s ability to effectively mitigate the impact of thermal noise, enabling reliable recovery of the global signal even under challenging observational scenarios. The robustness against such noise levels emphasizes the applicability of this method not only for SKA-1 but also for less sensitive instruments like MWA and LOFAR.

In Fig.8, We display the distribution of the correlation coefficient (CC) for the recovery from the 21cm PS including SKA-1 level thermal noise. Even with ther-

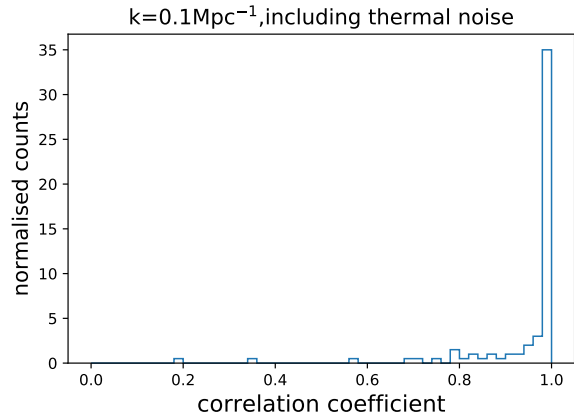


FIG. 8: Distribution of the correlation coefficient (CC) for the recovery from the 21cm PS with thermal noise. The mean value and variance of the CC are 0.83 and 0.15, respectively.

mal noise considered, most of the CC values exceed 0.8, closely resembling the distribution obtained when recovering the global signal from the 21cm PS without thermal noise. This result demonstrates that our ANN maintains high accuracy in reconstructing the global signal despite the presence of thermal noise.

The mean CC value of 0.83 and its variance of 0.15 quantitatively illustrate the resilience of the ANN-based recovery method to observational noise. Such robustness is particularly significant for practical applications, where thermal noise is unavoidable in real observational scenarios. The ability to achieve high recovery accuracy under these conditions emphasizes the suitability of ANN-based approaches for analyzing 21cm data from experiments like SKA-1. Furthermore, this capability supports the potential for cross-validation of recovered signals between interferometric and single-dish observations, enhancing the reliability of 21cm cosmological studies.

These results also underline the ANN’s potential to handle complex observational noise environments without significant loss of accuracy. The method’s consistent performance across varying noise levels reinforces its role as a robust tool for bridging different observational strategies and extracting meaningful cosmological information from noisy datasets.

To further assess the robustness of our method, we investigate whether the global signal from the cosmic dawn to the EoR can be reconstructed using only the 21cm PS at redshifts corresponding to the EoR. Specifically, we use the 21cm PS (without thermal noise) at redshifts $z = 7.5 - 15$, corresponding to the EoR, and at multiple wavenumbers ($k = 0.1 - 1.0\text{Mpc}^{-1}$, divided into 30 bins). In this scenario, the input to the ANN consists of the 21cm PS limited to $z = 7.5 - 15$, while the output layer still covers the broader redshift range $z = 7.5 - 35$ for the global signal. The total number of input neurons is 2310 (77 redshift bins \times 30 wavenumber bins), adjusted to match the reduced redshift range of the input PS.

In Fig. 9, we present examples of the recovered global signal using only the 21cm PS during the EoR. This figure evaluates whether the power spectrum at EoR redshifts contains sufficient information to reconstruct the global signal over a broader redshift span. For one specific model, the ANN successfully reconstructs the global signal across the redshift range, suggesting that certain astrophysical processes during the EoR leave a strong imprint on the power spectrum that correlates with the evolution of the global signal. However, the ANN fails to accurately reconstruct the global signal for another model, indicating that the EoR PS alone does not always encode sufficient information about earlier epochs.

In Fig.10, we show the distribution of the correlation coefficient (CC) for all test datasets in this scenario. The distribution reveals a mean CC value of 0.774 with a variance of 0.0677, indicating moderate success overall. However, the wide spread of CC values highlights significant variability among individual models. For certain models, high CC values (close to 1) suggest that the 21cm power spectrum during the EoR contains sufficient information to infer the global signal from cosmic dawn. This is likely due to strong correlations between astrophysical processes during reionization, such as X-ray heating or early star formation, and the thermal and ionization history of the intergalactic medium (IGM) during cosmic dawn. In these cases, large-scale features in the EoR PS, such as ionization bubbles, act as effective proxies for earlier cosmic conditions. Conversely, lower CC values observed for some models indicate that the 21cm PS at the EoR alone does not always encode the necessary information for accurate reconstruction. This discrepancy can arise in scenarios where the processes governing the 21cm PS during reionization are weakly coupled to the thermal evolution of the IGM at earlier epochs. For example, rapid reionization or minimal X-ray heating may reduce the imprint of cosmic dawn on the 21cm PS at the EoR, resulting in less informative features.

V. SUMMARY & DISCUSSION

In this paper, we have introduced a novel method to recover the global 21cm signal from the 21cm power spectrum using an artificial neural network (ANN). Our approach leverages the ANN’s ability to learn complex, non-linear mappings between the power spectrum and the global signal, offering a new pathway for analyzing the 21cm signal across a wide range of redshifts. This method demonstrates robustness against thermal noise and various astrophysical scenarios, making it a versatile tool for cosmological studies.

Our results show that the ANN-based method can accurately recover the 21cm global signal over a broad redshift range ($z = 7.5-35$). The recovered signals exhibit a high correlation with the true signals, with correlation coefficients (CC) typically above 0.8, even when realistic thermal noise levels, such as those expected for SKA-1,

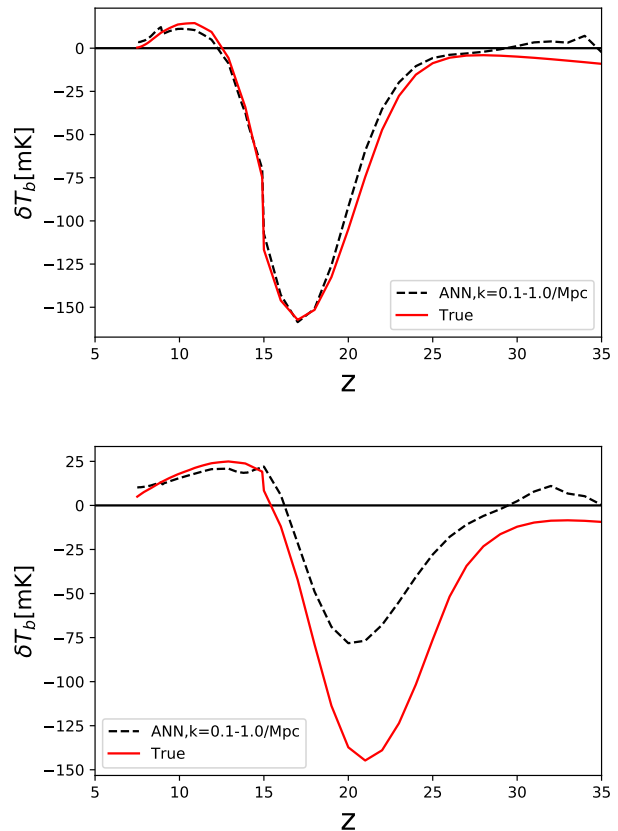


FIG. 9: Examples of the recovered 21cm global signal using the 21cm line power spectrum during the EoR at $z = 7.5-15$. The *red solid line* represents the target global signal, while the *black dashed line* shows the recovered signal from the EoR PS.

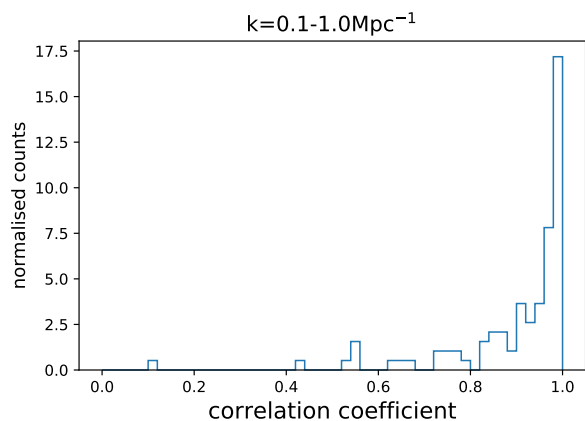


FIG. 10: Distribution of the correlation coefficient (CC) for all test datasets when recovering the global signal using the 21cm PS during the EoR. The mean CC is 0.774, and the variance is 0.0677.

are included. Specifically, as demonstrated in Figure 8, the inclusion of thermal noise does not significantly degrade the recovery accuracy, indicating the robustness of our method in practical observational scenarios.

One of the significant contributions of our method is its potential to independently validate results from single-dish experiments like EDGES. The deep 21cm absorption feature reported by EDGES has led to substantial debate. Our ANN-based method offers an independent way to extract the global signal from interferometric data, providing crucial cross-validation that could confirm or refute such unexpected findings. This capability is significant for resolving discrepancies between different observational techniques.

Furthermore, our analysis indicates that the recovery accuracy depends on the scales of the 21cm power spectrum employed. Larger scales (lower k values) contain more relevant information about the global signal, as small-scale fluctuations average out in the sky-averaged signal. We demonstrated that using the 21cm power spectrum at smaller scales alone is insufficient for accurate recovery, emphasizing the importance of incorporating larger scales to improve the ANN's performance across various Epoch of Reionization (EoR) models.

Our findings also reveal that the global signal can be reconstructed using the 21cm power spectrum from a limited redshift range during the EoR. As shown in Figure 9, the ANN successfully recovers the global signal across a broader redshift span in some cases, suggesting that the 21cm power spectrum at EoR redshifts contains sufficient information to infer the global signal from earlier epochs. However, this is not universally applicable to all models; the recovery's effectiveness depends on the specific char-

acteristics of the astrophysical model.

However, our study also faces certain limitations. The accuracy of the recovered 21cm global signal is contingent upon the quality and diversity of the training data used for the ANN. While our method has shown robustness against various types of observational noise, systematic errors inherent in real-world data could still pose significant challenges. For instance, astrophysical foregrounds, instrumental calibration errors, and ionospheric distortions may introduce complexities not fully captured in our simulations. Future research should focus on refining the generalization capabilities of the ANN by exploring a broader range of cosmological models and developing strategies to mitigate these systematic effects.

In conclusion, our ANN-based method represents a significant advancement in the field of 21cm cosmology. Offering a novel approach to recover the global signal from the power spectrum, not only facilitates cross-validation of observational results but also opens up new avenues for exploring the early Universe. The ability to recover the global signal using interferometric data addresses a critical challenge in 21cm cosmology, where different observational strategies can now be unified under a common analytical framework.

Acknowledgements

We appreciate Yi Mao's for useful comments and Anastasia Fialkov for providing simulation datasets. This work is supported by the National SKA Program of China (No.2020SKA0110401) and NSFC (Grant No. 12103044).

-
- [1] R. Barkana and A. Loeb, *Phys. Rep.* **349**, 125 (2001), astro-ph/0010468.
 - [2] S. R. Furlanetto, S. P. Oh, and F. H. Briggs, *Phys. Rep.* **433**, 181 (2006), astro-ph/0608032.
 - [3] D. Scott and M. J. Rees, *MNRAS* **247**, 510 (1990).
 - [4] P. Madau, A. Meiksin, and M. J. Rees, *ApJ* **475**, 429 (1997), astro-ph/9608010.
 - [5] J. R. Pritchard and A. Loeb, *Reports on Progress in Physics* **75**, 086901 (2012), 1109.6012.
 - [6] M. P. van Haarlem, M. W. Wise, A. W. Gunst, G. Heald, J. P. McKean, J. W. T. Hessels, A. G. de Bruyn, R. Nijboer, J. Swinbank, R. Fallows, et al., *A&A* **556**, A2 (2013), 1305.3550.
 - [7] R. B. Wayth, S. J. Tingay, C. M. Trott, D. Emrich, M. Johnston-Hollitt, B. McKinley, B. M. Gaensler, A. P. Beardsley, T. Booler, B. Crosse, et al., *PASA* **35**, 33 (2018), 1809.06466.
 - [8] D. R. DeBoer, A. R. Parsons, J. E. Aguirre, P. Alexander, Z. S. Ali, A. P. Beardsley, G. Bernardi, J. D. Bowman, R. F. Bradley, C. L. Carilli, et al., *PASP* **129**, 045001 (2017), 1606.07473.
 - [9] H. Shimabukuro, K. Hasegawa, A. Kuchinomachi, H. Yajima, and S. Yoshiura, *PASJ* **75**, S1 (2023), 2303.07594.
 - [10] G. Mellema, L. V. E. Koopmans, F. A. Abdalla, G. Bernardi, B. Ciardi, S. Daiboo, A. G. de Bruyn, K. K. Datta, H. Falcke, A. Ferrara, et al., *Experimental Astronomy* **36**, 235 (2013), 1210.0197.
 - [11] L. Koopmans, J. Pritchard, G. Mellema, J. Aguirre, K. Ahn, R. Barkana, I. van Bemmell, G. Bernardi, A. Bonaldi, F. Briggs, et al., *Advancing Astrophysics with the Square Kilometre Array (AASKA14) 1* (2015), 1505.07568.
 - [12] J. D. Bowman, A. E. E. Rogers, R. A. Monsalve, T. J. Mozdzen, and N. Mahesh, *Nature* **555**, 67 (2018), 1810.05912.
 - [13] D. C. Price, L. J. Greenhill, A. Fialkov, G. Bernardi, H. Garsden, B. R. Bardsell, J. Kocz, M. M. Anderson, S. A. Bourke, J. Craig, et al., *MNRAS* **478**, 4193 (2018), 1709.09313.
 - [14] L. Philip, Z. Abdurashidova, H. C. Chiang, N. Ghazi, A. Gumba, H. M. Heilgendorff, J. M. Jáuregui-García, K. Malepe, C. D. Nunhokee, J. Peterson, et al., *Journal of Astronomical Instrumentation* **8**, 1950004 (2019), 1806.09531.
 - [15] S. Singh, R. Subrahmanyam, N. Udaya Shankar, M. Sathyanarayana Rao, A. Fialkov, A. Cohen,

- R. Barkana, B. S. Girish, A. Raghunathan, R. Somashekar, et al., *ApJ* **858**, 54 (2018), 1711.11281.
- [16] J. Nambissan T., R. Subrahmanyam, R. Somashekar, N. Udaya Shankar, S. Singh, A. Raghunathan, B. S. Girish, K. S. Srivani, and M. Sathyanarayana Rao, arXiv e-prints arXiv:2104.01756 (2021), 2104.01756.
- [17] R. S. Polidan, J. O. Burns, A. Ignatiev, A. Hegedus, J. Pober, N. Mahesh, T.-C. Chang, G. Hallinan, Y. Ning, and J. Bowman, *Advances in Space Research* **74**, 528 (2024), 2404.03840.
- [18] S. D. Bale, N. Bassett, J. O. Burns, J. Dorigo Jones, K. Goetz, C. Hellum-Bye, S. Hermann, J. Hibbard, M. Maksimovic, R. McLean, et al., arXiv e-prints arXiv:2301.10345 (2023), 2301.10345.
- [19] M. Sathyanarayana Rao, S. Singh, S. K. S., G. B. S., K. Sathish, R. Somashekar, R. Agaram, K. Kavitha, G. Vishwapriya, A. Anand, et al., *Experimental Astronomy* **56**, 741 (2023).
- [20] X. Chen, J. Yan, L. Deng, F. Wu, L. Wu, Y. Xu, and L. Zhou, *Philosophical Transactions of the Royal Society of London Series A* **379**, 20190566 (2021), 2007.15794.
- [21] X. Chen, F. Gao, F. Wu, Y. Zhang, T. Wang, W. Liu, D. Zou, F. Deng, Y. Gong, K. He, et al., arXiv e-prints arXiv:2403.16409 (2024), 2403.16409.
- [22] R. Barkana, *Nature* **555**, 71 (2018), 1803.06698.
- [23] A. Fialkov and R. Barkana, *MNRAS* **486**, 1763 (2019), 1902.02438.
- [24] A. Parsons, J. Pober, M. McQuinn, D. Jacobs, and J. Aguirre, *ApJ* **753**, 81 (2012), 1103.2135.
- [25] A. Liu, J. R. Pritchard, M. Tegmark, and A. Loeb, *Phys. Rev. D* **87**, 043002 (2013), 1211.3743.
- [26] M. E. Presley, A. Liu, and A. R. Parsons, *ApJ* **809**, 18 (2015), 1501.01633.
- [27] B. McKinley, C. M. Trott, M. Sokolowski, R. B. Wayth, A. Sutinjo, N. Patra, T. J. Nambissan, and D. C. X. Ung, *MNRAS* **499**, 52 (2020), 2009.06146.
- [28] X. Zhang, B. Yue, Y. Shi, F. Wu, and X. Chen, *ApJ* **945**, 109 (2023), 2301.12223.
- [29] A. Cohen, A. Fialkov, and R. Barkana, *MNRAS* **478**, 2193 (2018), 1709.02122.
- [30] A. Fialkov, R. Barkana, and M. Jarvis, *MNRAS* **491**, 3108 (2020), 1904.10857.
- [31] H. Shimabukuro and B. Semelin, *MNRAS* **468**, 3869 (2017), 1701.07026.
- [32] N. Gillet, A. Mesinger, B. Greig, A. Liu, and G. Ucci, *MNRAS* **484**, 282 (2019), 1805.02699.
- [33] A. Doussot, E. Eames, and B. Semelin, *MNRAS* **490**, 371 (2019), 1904.04106.
- [34] N. S. Kern, A. Liu, A. R. Parsons, A. Mesinger, and B. Greig, *ApJ* **848**, 23 (2017), 1705.04688.
- [35] C. J. Schmit and J. R. Pritchard, *MNRAS* **475**, 1213 (2018), 1708.00011.
- [36] W. D. Jennings, C. A. Watkinson, F. B. Abdalla, and J. D. McEwen, *MNRAS* **483**, 2907 (2019), 1811.09141.
- [37] A. Cohen, A. Fialkov, R. Barkana, and R. A. Monsalve, *MNRAS* **495**, 4845 (2020), 1910.06274.
- [38] S. Yoshiura, H. Shimabukuro, K. Hasegawa, and K. Takahashi, *MNRAS* **506**, 357 (2021), 2004.09206.
- [39] W. Li, H. Xu, Z. Ma, R. Zhu, D. Hu, Z. Zhu, J. Gu, C. Shan, J. Zhu, and X.-P. Wu, *MNRAS* **485**, 2628 (2019), 1902.09278.
- [40] H. Shimabukuro, Y. Mao, and J. Tan, *Research in Astronomy and Astrophysics* **22**, 035027 (2022), 2002.08238.
- [41] X. Zhao, Y. Mao, C. Cheng, and B. D. Wandelt, *ApJ* **926**, 151 (2022), 2105.03344.
- [42] X. Zhao, Y. Mao, and B. D. Wandelt, *ApJ* **933**, 236 (2022), 2203.15734.
- [43] A. Cohen, A. Fialkov, R. Barkana, and M. Lotem, *MNRAS* **472**, 1915 (2017), 1609.02312.
- [44] D. E. Rumelhart, G. E. Hinton, and R. J. Williams, *Nature* **323**, 533 (1986).
- [45] M. McQuinn, O. Zahn, M. Zaldarriaga, L. Hernquist, and S. R. Furlanetto, *Astrophys. J.* **653**, 815 (2006).
- [46] Y. Mao, M. Tegmark, M. McQuinn, M. Zaldarriaga, and O. Zahn, *Phys. Rev. D* **78**, 023529 (2008).
- [47] Y. Mao, A. D'Aloisio, J. Zhang, and P. R. Shapiro, *Phys. Rev. D* **88**, 081303 (2013), 1305.0313.
- [48] A. Lidz, S. R. Furlanetto, S. P. Oh, J. Aguirre, T.-C. Chang, O. Doré, and J. R. Pritchard, *ApJ* **741**, 70 (2011), 1104.4800.
- [49] A. Mesinger, A. Ewall-Wice, and J. Hewitt, *MNRAS* **439**, 3262 (2014), 1310.0465.